# UC Irvine
## UC Irvine Previously Published Works


### Title
Ultrathin Titanium Nitride Epitaxial Structures for Tunable Infrared Plasmonics


### Permalink
https://escholarship.org/uc/item/42r3r06d



### Journal
The Journal of Physical Chemistry C, 127(43)

### ISSN
1932-7447



### Authors
Chang, Ching-Wen
Huang, Chiao-Tzu
Wu, Jhih-Sheng
et al.



### Publication Date
2023-11-02

### DOI
10.1021/acs.jpcc.3c04763



### Copyright Information
This work is made available under the terms of a Creative Commons Attribution License, available at https://creativecommons.org/licenses/by/4.0/

Peer reviewed

eScholarship.org Powered by the California Digital Library
University of California

THE JOURNAL OF PHYSICAL CHEMISTRY C
A JOURNAL OF THE AMERICAN CHEMICAL SOCIETY
pubs.acs.org/JPCC
Article

# Ultrathin Titanium Nitride Epitaxial Structures for Tunable Infrared Plasmonics

*Published as part of The Journal of Physical Chemistry C virtual special issue "Hiroaki Misawa Festschrift".*

Ching-Wen Chang,* Chiao-Tzu Huang, Jhih-Sheng Wu, Zih-Hao Song, Chih-Hsuan Liao, Quynh T. Dang, Yu-Jung Lu, Ho Wai Howard Lee, Hyeyoung Ahn, and Shangjr Gwo*

Cite This: J. Phys. Chem. C 2023, 127, 21186−21193
Read Online

ACCESS | Metrics & More | Article Recommendations | Supporting Information

**ABSTRACT:** Titanium nitride (TiN) is an ideal material for infrared plasmonics due to its excellent optical properties, high melting temperature, mechanical and chemical stabilities, and bio- and CMOS compatibilities. In this work, we demonstrate that ultrathin and scalable TiN epitaxial structures can be applied for tunable infrared plasmonics, extending into near- to mid-infrared spectral regions. The ultrathin (111)-oriented TiN epitaxial films studied here were grown on *c*-plane sapphire wafers without any wetting layer by ultrahigh-vacuum nitrogen-plasma-assisted molecular-beam epitaxy. This method allows for stoichiometric TiN growth without the issue of contamination (especially oxygen) in conventional TiN growth techniques. Structural analyses for these films validate their single-crystalline properties with continuous film morphologies down to a few nanometers in thickness. Furthermore, the frequency-tunable (wavelength range: 1−4 μm) plasmonic metasurfaces have been demonstrated by controlling surface plasmon resonances via lithographically patterning of ultrathin TiN epitaxial films with varying thicknesses (4−30 nm) and grating structure parameters (pitch: 300−1200 nm, width: 200−800 nm). The tunable plasmonic metasurfaces based on ultrathin TiN epitaxial films hold great promise for emerging infrared plasmonic applications, such as thermal photovoltaics requiring narrow-band emitters, photodetectors, and biosensors in the near- and mid-infrared spectral regions.

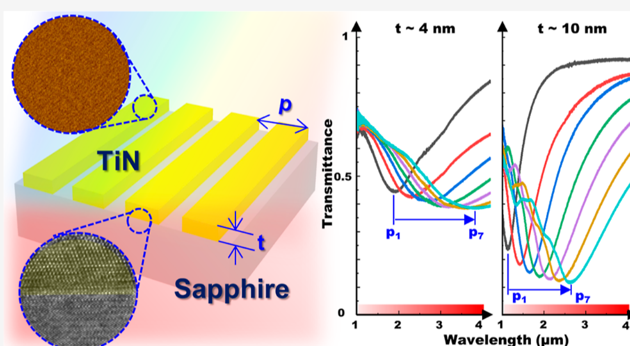


Downloaded via UNIV OF CALIFORNIA IRVINE on April 9, 2024 at 17:15:07 (UTC).
See https://pubs.acs.org/sharingguidelines for options on how to legitimately share published articles.

## ■ INTRODUCTION

The infrared (IR) spectral region covers the electromagnetic radiation with wavelengths longer than the visible light (>700 nm) and shorter than the microwave wavelengths (<1 mm). The IR region can be further divided into near-infrared (NIR), mid-infrared (MIR), and far-infrared (FIR) regions. Among them, the NIR subwindow (1.5 to 2 μm) and the MIR (2 to 6 μm) region are particularly useful for optical imaging/detection, biochemical sensing, and environmental monitoring. These advantages originate from relatively low water absorption and light scattering for optical imaging/detection and the spectral locations of optical "fingerprints" for most of common gases and biomolecules in infrared vibrational spectroscopy. However, the IR region has been quite challenging for photonic applications since the detectors and emitters made from narrow-bandgap semiconductors are intrinsically less efficient and noisy. The situation changes dramatically following the introduction of intersubband devices such as quantum cascade lasers[1] and superconducting nanowire single-photon detectors.[2,3] Moreover, the recent developments of plasmonic materials and devices for light localization, enhancement, and manipulation[4−6] have opened up new opportunities for infrared plasmonics.[7−12]

In plasmonic applications, the most used plasmonic materials are noble metals, especially gold (Au) and silver (Ag), which have good plasmonic properties in the visible and NIR spectral range. However, they have significant material issues such as incompatibility with CMOS processing (Au, Ag), biotoxicity (Ag), and lack of thermal (Au, Ag), mechanical (Au, Ag), and chemical (Ag) stabilities. For these reasons, alternative plasmonic materials have been proposed and studied,[13] including those suitable for IR plasmonics.[7−12,14−17] To date, there are several possible IR plasmonic materials, including transparent conducting oxides,[7,12,13] graphene,[9−11] conducting transition-metal nitrides

Received: July 14, 2023
Revised: September 23, 2023
Published: October 18, 2023

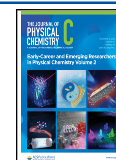

ACS Publications © 2023 American Chemical Society



https://doi.org/10.1021/acs.jpcc.3c04763
J. Phys. Chem. C 2023, 127, 21186−21193

(TMNs),[14−17] silicides,[11] and doped semiconductors.[11] Among them, graphene is a representative two-dimensional plasmonic material with a unique band structure and very high mobility. Besides, it has been reported that graphene is a promising low-loss MIR plasmonic material with spectral tunability of plasmonic response via gate biasing or chemical doping.[9−11] However, limited carrier concentrations in graphene have prevented the graphene plasmonics into the NIR and visible wavelength ranges.[11]

To overcome this limitation, Maniyara et al. demonstrated electrically tunable plasmonics for 1.5−5 μm resonance wavelengths in ultrathin (a few nanometers) Au films with reduced surface charges, in contrast to their large bulk carrier density.[18] Abd El-Fattah et al. reported lithographically patterned wafer-scale ultrathin Ag crystalline films for plasmonic applications in the NIR and MIR ranges.[19] Unfortunately, Au and Ag are not suitable for refractory plasmonic applications due to their low melting temperatures and mechanical strengths. In comparison, conducting TMNs possess unique material characteristics, which allow for refractory plasmonic applications under high temperature, high power, mechanically hard, and corrosion-resistant operational conditions.[20−26] In particular, titanium nitride (TiN) has a high melting point (∼3000 °C), as well as the highest electrical conductivity among TMNs and excellent plasmonic properties for optical[14−17,22−26] and biomedical[27,28] applications.

Furthermore, TiN can be used to overcome the challenge of depositing ultrathin, continuous metal films because typical metals have high surface energies due to the presence of unsaturated dangling bonds. It is well-known that noble metals, such as Au and Ag do not properly wet on most of the available substrates below the percolation threshold thickness (<10 nm), resulting in discontinuous and polycrystalline thin films with large surface roughness and atomically diffused interfaces.[29] Therefore, deposition of ultrathin metal films typically requires additional wetting layers,[18] resulting in increased optical losses and other device compatibility issues.[30] Therefore, special growth techniques, such as growth at cryogenic temperatures[19,30] or on special substrates,[31] are necessary to prepare ultrathin metal films without wetting layers. In this aspect, TiN offers an excellent opportunity for epitaxial growth of metals on semiconductor or oxide substrates because they have a mixture of covalent and metallic bonding.[29]

Here, we demonstrate wetting-layer-free, ultrathin TiN epitaxial (single-crystalline) films on sapphire with thicknesses down to 4 nm, which were grown by ultrahigh-vacuum (UHV) nitrogen ($N_2$)-plasma-assisted molecular-beam epitaxy (MBE). The MBE growth method enables growth of stoichiometric (oxygen-free) ultrathin TiN epitaxial films with excellent plasmonic properties. By using these films, we were able to realize spectrally tunable TiN plasmonic metasurfaces with quality factors comparable to those achieved by using Au and Ag ultrathin films and with a wider spectral range. The ultrathin TiN metasurfaces demonstrated here can be used as a tunable plasmonic material platform for both tunable plasmonics[32−37] and epsilon-near-zero[38−42] applications. Compared to previous optical studies based on ultrathin TiN films,[32−34] the major difference is that we used ultrathin TiN films grown by MBE for the present study (in contrast to conventional TiN films grown by reactive sputter deposition), which can have better film interface control and material properties at high temperatures for refractor plasmonic applications, as demonstrated by our previous work, where we compared the performance of MBE-grown TiN plasmonic structures vs reactive-sputter-grown TiN plasmonic structures.[25]

## ■ METHODS

**Epitaxial Growth of Ultrathin TiN Films on Sapphire Wafers.** The epitaxial growth of TiN(111) ultrathin films on 2 in. *c*-plane sapphire wafers was carried out by a nitrogen-plasma-assisted MBE system equipped with a radio frequency (RF) plasma source. The ultrahigh vacuum base pressure was kept at $1 \times 10^{-10}$ Torr before growth. Double-side polished sapphire wafers were cleaned with acetone, isopropanol, and deionized water in an ultrasonic bath to remove organic contaminations and then dehydrated by nitrogen gas. Prior to the TiN(111) epitaxial growth, the sapphire wafer was thermally degassed at 950 °C for 2 h to prepare a clean surface exhibiting a streaky reflection high-energy electron diffraction (RHEED) pattern. The elemental titanium (Ti) beam with $1 \times 10^{-8}$ Torr beam equivalent pressure was provided by a solid-source (Ti with 5N purity) effusion cell. A purified 7 N nitrogen flux was controlled via a high-resolution mass flow controller.

**Fabrication of Ultrathin TiN Nanoribbon Arrays.** The TiN nanoribbon arrays were fabricated on double-sided polished *c*-sapphire by using electron beam lithography (EBL). Hexamethyldisilazane (HDMS) and diluted ZEP520A photoresist were spin-coated onto the cleaned TiN thin film, sequentially. Nanoribbons were then written using an electron-beam lithography system (Elionix ELS-7500) under an electron dose value of 140 $\mu C/cm^2$ (beam current: 100 pA, beam voltage: 50 kV), followed by development in amyl acetate for 2 min and rinsing in isopropanol for 30 s. Then, a dry etching process was used to transfer the nanoribbon structure to the TiN device layer in chlorine-based inductively coupled plasma at 400 W. Finally, the residual photoresist was removed by *N*-methyl-2-pyrrolidone (NMP), isopropyl alcohol (IPA), and deionized water rinsing.

**Structural Characterization.** The crystal properties of TiN epitaxial films were analyzed by using high-resolution X-ray diffraction (Bede D1, HR-XRD) with a Cu $K_{\alpha 1}$ X-ray source (1.54052 Å), while the surface morphologies of thin films were inspected by scanning electron microscopy (SEM, JEOL JSM-7000F) and atomic force microscopy (AFM, Bruker Dimension). The atomic-resolution lattice images were acquired by high-resolution transmission electron microscopy (HR-TEM, JEOL JEM-F200) operated at 200 kV electron beam energy.

**Electrical Characterization.** The 1 $cm^2$-square, ultrathin TiN epitaxial film was patterned with four indium contacts at its corners for electrical characterization. We used indium balls as contact electrodes, which were melted by a soldering iron at 200 °C. We found that indium can diffuse to the TiN surface to obtain good ohmic contacts. The sheet resistance and Hall effect measurements of the TiN film were measured by using the four-point, Van der Pauw technique in a magnetic field of 0.52 T at room temperature.

**Optical Measurement Setup.** Optical transmission spectra were measured by using a Fourier-transform infrared spectrometer (FTIR, Bruker VERTEX 70) coupled to an infrared microscope (Bruker HYPERION 3000). The infrared microscope is equipped with a 36× reflective microscope objective (Newport 50102-02, numerical aperture: 0.52),


https://doi.org/10.1021/acs.jpcc.3c04763
J. Phys. Chem. C 2023, 127, 21186−21193

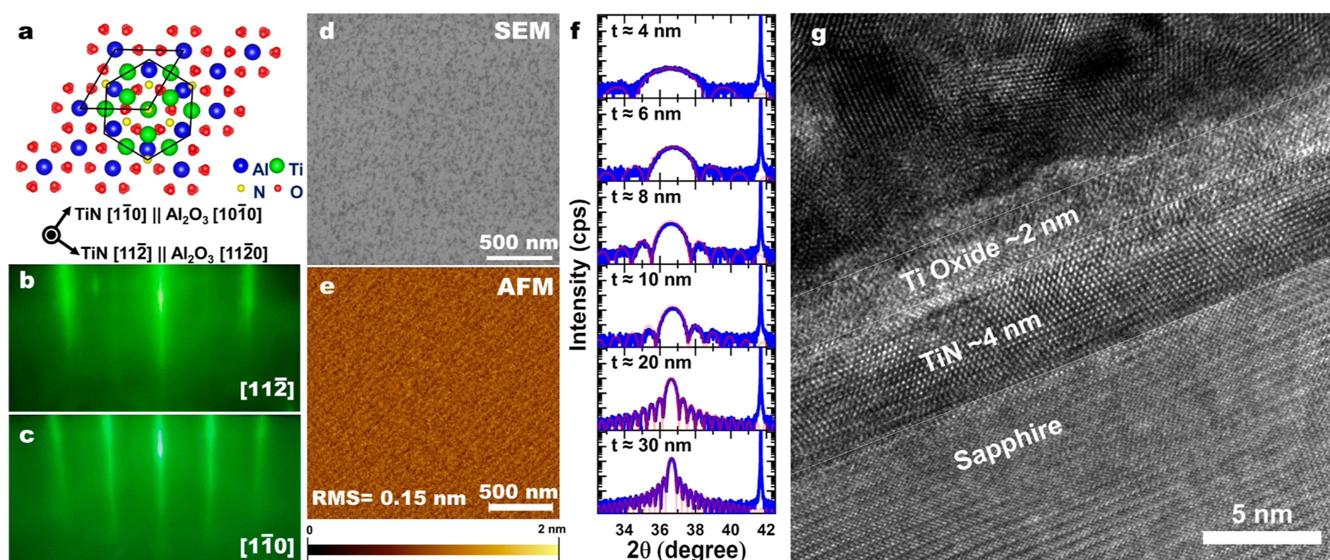


**Figure 1.** (a) Schematic illustration of in-plane atomic arrangement in the case of TiN epitaxial layer grown on *c*-sapphire. The RHEED patterns were obtained (b) along TiN [11$\bar{2}$] and (c) TiN [1$\bar{1}$0] azimuthal directions. (d) SEM top-view image of the 4 nm TiN ultrathin film. (e) AFM image showing the surface morphology of the 4 nm TiN ultrathin film. (f) X-ray diffractograms ($\omega-2\theta$ scans at the (111) reflection) of ultrathin TiN layers. The TiN layer thicknesses are numerically fitted by using the satellite fringes. The red line is fittings to the experimental results (blue line). The thinnest TiN film is about 4 nm. (g) TEM image of 4 nm TiN shows the formation of abrupt heterointerfaces. A ~2 nm-thick native oxide (titanium oxide) layer formed on top of the 4 nm TiN layer upon air exposure of the MBE-grown TiN film. The titanium oxide layer forms a diffusion barrier to prevent further oxidation.

which has a 0.5 mm field of view and a wide spectral range (200 nm to 20 mm). However, this reflective objective collects the light with a 15−30° incident angle. Therefore, strictly speaking, the light collection geometry is only approximately normal incidence. As a result, simulation results using the normal incidence conditions can be merely used for understanding the mechanism and not for a direct comparison with the experimental data. A linearly polarized light was aligned transversally to the orientation of TiN nanoribbons via infrared polarizers (LPNIR100 for 1−2 $\mu$m wavelength and LPMIR100 for 2−5 $\mu$m wavelengths) to excite the plasmonic resonances in TiN nanoribbon arrays.

## ■ RESULTS AND DISCUSSION

It is known that titanium is an active absorbing agent and getter material that has been widely used as a sublimation pump material in UHV systems. Therefore, conventional TiN films prepared by reactive sputtering or chemical vapor deposition have a high propensity to form titanium oxynitride and other forms of nonstoichiometric titanium nitride films. Recently, the growth of stoichiometric TiN epitaxial films[17,24−26,35,36] has reported to be feasible by using the MBE method in an UHV environment. In this work, ultrathin TiN epitaxial films were grown by nitrogen-plasma-assisted MBE (see details in Methods) on *c*-plane sapphire substrates without any wetting layer due to a mixture of covalent and metallic bonding in the TiN rock-salt structure.[29]

**Structural Characterization.** Figure 1a schematically shows that the [111]-oriented TiN film with the rock-salt structure can be grown on [0001]-oriented (*c*-plane) sapphire substrates with the following epitaxial relationships: TiN[111]‖ sapphire [0001], TiN[1$\bar{1}$0]‖sapphire[10$\bar{1}$0], and TiN[11$\bar{2}$]‖ sapphire[11$\bar{2}$0]. In situ streaky RHEED patterns shown in Figure 1b,c for the case of the 4 nm thick TiN film confirm the epitaxial relationships and indicate the formation of atomically smooth TiN film morphology. In this work, TiN(111) epitaxial films with different thicknesses (4, 6, 8, 10, 20, and 30 nm) were grown by MBE under stoichiometric conditions at a 20 nm/h growth rate.

Furthermore, the film morphologies were examined by ex situ SEM and AFM, as shown in Figure 1d,e for the case of the 4 nm-thick TiN film (additional data are shown in Figure S1 for other TiN films). When the film thickness is increased to 30 nm, nucleated TiN triangular islands can be observed. Figure 1e shows that the 4 nm-thick TiN film has a surface roughness ~0.15 nm, as measured by AFM under a scan size of 2 × 2 $\mu m^2$. The comparison of TiN with different thicknesses (from 4 to 30 nm) based on 1 $\mu m^2$ scan area is shown in Figure S2, which confirms the surface roughness less than 0.5 nm for all cases.

For large-scale structural analysis, XRD $\omega-2\theta$ rocking curves for ultrathin TiN films with different thicknesses are shown in Figure 1f. The XRD peak centered at around 36.65° corresponds to the TiN (111) peak, while another one at 41.685° originated from the *c*-plane sapphire (0006) peak. Clear XRD peaks from ultrathin TiN films confirm the high crystalline quality of MBE-grown samples, while the broadening of peak width is due to the size (thickness) effects of ultrathin films. The satellite interference fringes (*Pendellösung* fringes) in the XRD curves can be used to estimate the film thickness via the interference fringe periods. Using this method, the TiN thicknesses can be identified to be 4, 6, 8, 10, 20, and 30 nm, respectively. Using this method, the TiN thicknesses with ±5% deviation can be identified to be 4, 6, 8, 10, 20, and 30 nm, respectively. Additionally, the TiN thickness distribution in x−y plane for 6 and 10 nm is shown in Figure S3.

The cross-sectional TEM image shown in Figure 1g shows the formation of an abrupt interface between the TiN film and the sapphire substrate, and the high-resolution TEM images of the TiN region show that the (111) layer spacing is about 2.4 Å, consistent with the XRD data. The TEM analyses confirm a



https://doi.org/10.1021/acs.jpcc.3c04763
J. Phys. Chem. C 2023, 127, 21186−21193

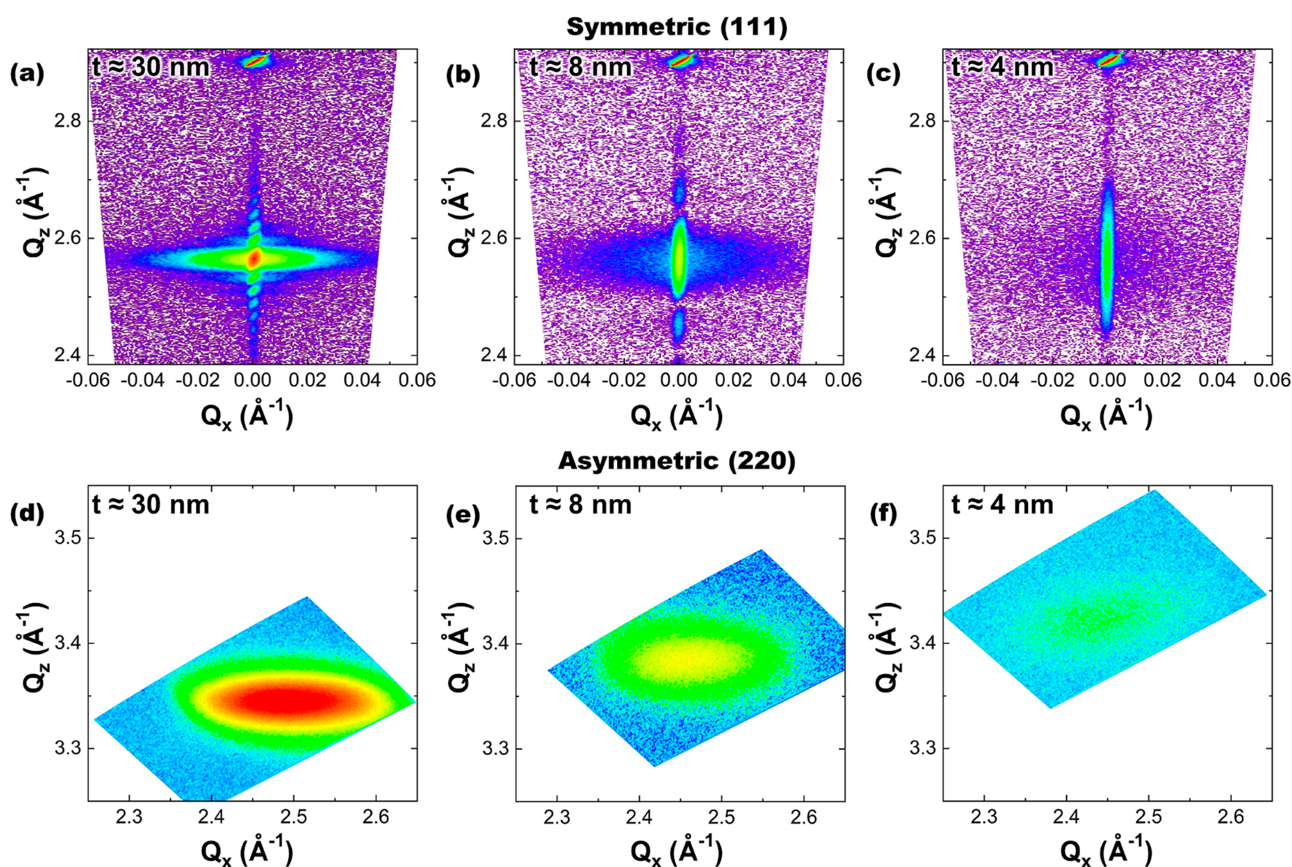


**Figure 2.** (a−c) symmetric and (d−f) asymmetric X-ray RSMs for 30, 8, and 4 nm TiN layers grown on *c*-sapphire.

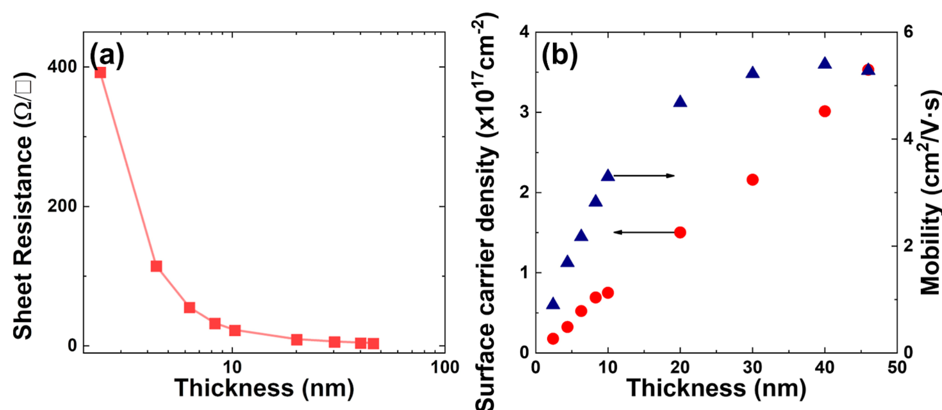


**Figure 3.** (a) Room-temperature electrical sheet resistance of TiN measured as a function of film thickness. (b) Thickness-dependent surface carrier density and carrier mobility of TiN films measured by the van der Pauw method.

close-packed rock-salt lattice structure in TiN films, where N atoms occupy octahedral interstitial sites in the Ti face-centered cubic lattice. In addition, the TEM image testifies the formation of a self-limited native titanium oxide passivation layer (∼2 nm thick) on the as-grown 4 nm-thick TiN film. An additional TEM image revealing a native oxide layer (∼1 nm thick) is shown in Figure S4. Furthermore, the selected area electron diffraction patterns obtained by TEM also indicate the same TiN/sapphire epitaxial relations: TiN$[1\bar{1}0]$||sapphire-$[10\bar{1}0]$ and TiN$[11\bar{2}]$||sapphire$[11\bar{2}0]$, as shown in Figure S5.

For more detailed characterization of the lattice constant and crystal structure, Figure 2 shows X-ray reciprocal space mapping (RSM) for 30, 8, and 4 nm thick TiN grown on *c*-plane sapphire under symmetric and asymmetric X-ray incident conditions. In symmetric scans shown in Figure 2a−c, a clear broadening of TiN(111) reciprocal lattice reflection intensity distribution and the observation satellite fringes toward $Q_z$ are due to thin film finite-size interference, which agrees well with the results obtained from the $\omega-2\theta$ scan. Besides, we can observe that the maximum reflection intensity of symmetric TiN(111) shifts to lower $Q_z$ and the asymmetric TiN(220) peaks shift to higher $Q_z$ values (Figure 2d−f), which are caused by compressive stress in ultrathin TiN films under epitaxial growth conditions on a sapphire substrate with a lattice mismatch. The interlayer spacing can be obtained for $d_{(111)}$ (out-of-plane) to be 2.450, 2.452, and 2.453 Å, as well as for $d_{(220)}$ (in-plane) to be 1.753, 1.749, and 1.746 Å from the RSM analyses for 30, 8, and 4 nm TiN(111) epitaxial films,


https://doi.org/10.1021/acs.jpcc.3c04763
J. Phys. Chem. C 2023, 127, 21186−21193

respectively. These results confirm the high-quality epitaxial growth of ultrathin TiN layers on the sapphire substrates. Furthermore, it shows that strain engineering can be a viable approach for future device applications based on epitaxially grown TiN ultrathin layers.

**Electrical Characterization.** The 1 $cm^2$ square samples of ultrathin TiN films were patterned with four indium contacts at their corners for electrical characterization. Before Hall measurements, we checked the contact $I-V$ curves with good linear behavior, and the results are shown in Figure S6 (Supporting Information). The sheet resistance and Hall effect measurements of TiN ultrathin films were measured by the four-point Van der Pauw method in a magnetic field of 0.52 T at room temperature. The sheet resistances of TiN ultrathin films are shown in Figure 3a, while the surface carrier densities and mobilities of TiN films with different thicknesses are shown in Figure 3b. The thinnest layer exhibits a sheet resistance of 392 Ω/□e. In comparison, sheet resistances of ultrathin TiN, Au, and Ag films with different film thicknesses are shown in Figure S7 (Supporting Information). For TiN films with thicknesses greater than 20 nm, the bulk properties can be reached (i.e., sheet resistance and mobility). The three-dimensional bulk carrier density can be evaluated to be 7−8 × $10^{22}$ $cm^{-3}$, and the two-dimensional surface carrier density $n_s = n_b t$, where $n_s$ is the surface carrier density, $n_b$ is the bulk carrier density, and $t$ is the film thickness, has a value of 2.9 × $10^{16}$ $cm^{-2}$ for the 4 nm-thick TiN layer. Thus, for the applications of electrical gating for tunable plasmonic resonances, ultrathin TiN epitaxial films can be a viable approach by choosing an appropriate layer thickness for the desired tuning range. This is a clear distinction in comparison with the cases of atomically thin plasmonic materials, such as graphene, with a limited range of carrier concentration. Notably, ultrathin TiN layers exhibit remarkable adhesion and structural stability, which can be quite advantageous for gate-tunable metasurface applications.

**Optical Characterization.** In solar cell applications, the Shockley−Queisser (SQ) limit is a theoretical upper bound of the solar energy conversion efficiency using a single semiconductor p−n junction. The SQ limitation originates from the broadband nature of the solar spectrum and the semiconductor bandgap: Photons are not absorbed if the incident photon energy is less than the semiconductor bandgap, while photons with energy greater than the bandgap are absorbed with some energy loss due to fast electron−hole pair relaxation to the band edges.[43] To overcome this limitation (broad solar spectrum), the concept of the solar thermophotovaltic (STPV) system has been proposed and demonstrated by including an intermediate light absorption (broadband)/emission (narrowband) element between the sunlight and the solar cell.[44−49] In essence, this intermediate element acts as an alternative "Sun" for solar cells,[45] which is designed to absorb the entire solar spectrum[17,25] and emit a narrowband spectrum tailored to match with the desired semiconductor photovoltaic element.[50] The utmost advantage of STPV is that all solar energy is converted into electrical energy and the overall conversion efficiency can be tremendously boosted.[47−49]

However, the progress of the SPTV system has been slow due to the lack of reliable and sustainable optical materials, which can operate at high temperatures. Recent advances in low-loss refractory plasmonic materials have provided new opportunities for SPTV developments. Especially, it has been experimentally demonstrated that TiN is an excellent refractory plasmonic material[21−23] for building optical broadband absorption and narrowband emitters. Particularly, TiN has been considered as the best plasmonic material for photothermal energy conversion applications over a broad spectral region of the solar spectrum.[25] According to the recent theoretical and experimental studies,[22] nanostructured TiN is an excellent broadband sunlight absorber due to strong plasmonic resonance ranging from 300 to 1300 nm, corresponding to the major sunlight spectral composition. One of the remaining major challenges is to develop a tunable thermal emitter with narrowband emission at a selective wavelength to match the bandgap of a bottom photovoltaic cell.[50] Here, we demonstrate that plasmonic metasurfaces consisting of ultrathin TiN nanoribbons can be used as the desired tunable thermal emitters with narrowband resonances for both NIR and MIR wavelength regions.

In Figure 4a, we show the schematic drawing of the TiN nanoribbon structure used for optical characterization, which has a fixed ratio between nanoribbon width $w$ and nanoribbon period $p$ ($p = 1.5w$). The SEM images in Figure 4a show patterned TiN thin film samples with seven different nanoribbon structural parameters. A total of 42 samples were measured with six different film thicknesses ($t$), varied from 4 to 30 nm. The localized surface plasmon resonances can be efficiently excited via illuminated with normally incident, linearly polarized (transverse magnetic mode) infrared light. For these measurements, the reference transmission spectrum was measured for bare sapphire under the same polarization conditions of incident light. In this study, the film permittivity (dielectric function) can be fitted by using the Drude model via the NIR and MIR transmittance spectra, as shown in Figure S8, and the detailed Drude parameters are presented in Table S1 (Supporting Information). Moreover, the visible range permittivity data of ultrathin TiN epitaxial films grown by MBE are presented in our previous work.[36]

Before showing the experimental results, we used the finite-difference time-domain (FDTD) simulation results under normal incidence conditions to demonstrate the feasibility of tunable plasmonics in the near- and mid-infrared spectral regions. The Drude damping factors $\gamma$ used in FDTD simulations are 0.49, 0.42, 0.29, 0.23, 0.23, and 0.20 eV for $t$ = 4, 6, 8, 10, 20, and 30 nm, respectively. The simulation results shown in Figure 4b−d are quite consistent with experimental results (transmittance spectra) in Figure 4e, showing tunable plasmonic resonances from the near- to mid-infrared region by modulating ribbon widths and using TiN ultrathin layers with different thicknesses. Besides the main peak observed in simulations and experimental spectra, an additional sideband can be observed. The main peak can be attributed to a first-order dipolar mode of localized plasmon resonance, while the small sideband is likely originated from a high-order resonance mode at higher energy. More detailed theoretical studies will be needed to clarify this point.

In Figure 5, we show the surface plasmon dispersion curves summarized by the experimental measurement results. The plasmonic dispersion curve obtained for the thicker films is closer to the light−line curve (solid red line) for the air/sapphire (substrate) interface. In contrast, due to stronger confinement effects, the surface plasmons of thinner films exhibit larger wavevectors (wavenumbers) at a fixed plasmon frequency. This is due to the coupling of surface plasmon at the upper and lower metal/dielectric interfaces of ultrathin


https://doi.org/10.1021/acs.jpcc.3c04763
J. Phys. Chem. C 2023, 127, 21186−21193

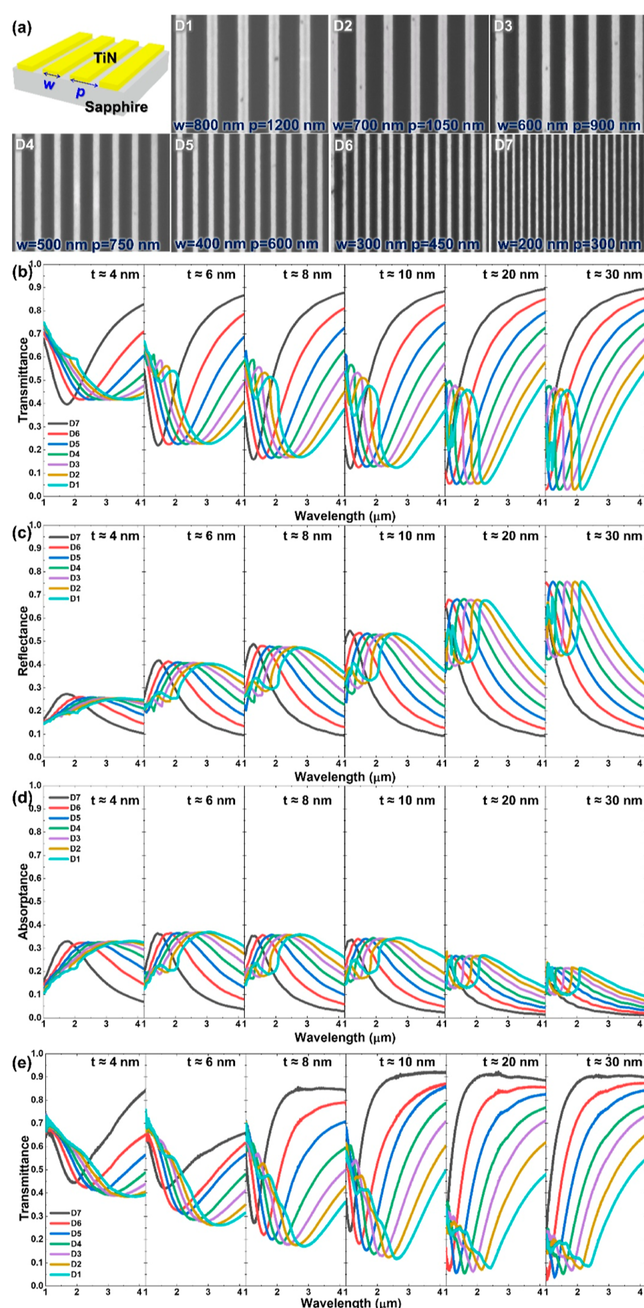


Figure 4. (a) Schematic illustration and SEM images of the grating structures (one-dimensional TiN nanoribbon arrays) fabricated from single-crystalline TiN ultrathin layers. In the SEM images, the darker regions correspond to the fabricated TiN ribbons. (b) FDTD-simulated transmittance spectra. (c) FDTD-simulated reflectance spectra. (d) FDTD-simulated absorptance spectra. (e) Experimentally measured transmittance spectra of TiN gratings, showing tunable plasmonic resonances from the near- to mid-infrared region by modulating ribbon widths and using TiN ultrathin layers with different thicknesses.

metal films. Therefore, stronger plasmon dispersion bending appears when the TiN films become thinner, as expected by film thickness dependence of surface plasmon coupling. In comparison with the plasmonic dispersions achieved with the ultrathin Au films,[18] we can obtain comparable quality factors ($Q$) of plasmon resonances (comparison is shown in Figure S9). Furthermore, the tuning range of the TiN case is wider. Most importantly, TiN can be applied to refractory plasmonic

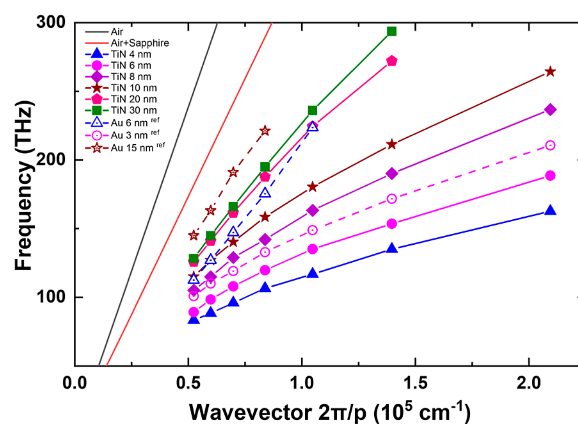


Figure 5. Comparison between experimental surface plasmon dispersion curves obtained for TiN and Au ultrathin gratings with different layer thicknesses. The Au data are reported by Maniyara et al. (ref 18).

applications. The results presented here clearly demonstrate that ultrathin TiN epitaxial films can be an excellent plasmonic material platform for tunable plasmonics in the near- and mid-infrared regions.

## CONCLUSIONS

In summary, broad tunable infrared spectral responses have been demonstrated for plasmonic metasurfaces fabricated by using ultrathin TiN epitaxial films grown on sapphire substrates by MBE. These ultrathin TiN films can be formed on sapphire without the dewetting issue of common plasmonic materials and possess excellent thermal, mechanical, and chemical stabilities. Taking advantage of these unique characteristics, ultrathin TiN plasmonic metasurfaces can be used in a variety of optical applications, such as transparent conductive electrodes, optical biosensing, solar energy harvesting, electro-optical tunable plasmonics, and metasurface-based nonlinear optics.

## ASSOCIATED CONTENT

### Supporting Information

The Supporting Information is available free of charge at https://pubs.acs.org/doi/10.1021/acs.jpcc.3c04763.

The Supporting Information includes SEM, AFM, and TEM images, additional XRD data, SAED patterns, electrical measurements, comparison of sheet resistances, near- and mid-infrared transmittance spectra, comparison of quality factors, and Drude model parameters (PDF)

## AUTHOR INFORMATION

### Corresponding Authors

**Shangjr Gwo** − *Research Center for Applied Sciences, Academia Sinica, Taipei 11529, Taiwan; Institute of NanoEngineering and MicroSystem, National Tsing-Hua University, Hsinchu 30013, Taiwan; Department of Physics, National Tsing-Hua University, Hsinchu 30013, Taiwan;* orcid.org/0000-0002-3013-0477; Email: gwo@phys.nthu.edu.tw

**Ching-Wen Chang** − *Research Center for Applied Sciences, Academia Sinica, Taipei 11529, Taiwan;* orcid.org/0000-0002-1748-4983; Email: cwchang@phys.nthu.edu.tw



https://doi.org/10.1021/acs.jpcc.3c04763
J. Phys. Chem. C 2023, 127, 21186−21193

### Authors

**Chiao-Tzu Huang** − *Department of Electrophysics, National Yang-Ming Chaio-Tung University, Hsinchu 30010, Taiwan;* orcid.org/0000-0002-1396-4605

**Jhih-Sheng Wu** − *Department of Photonics, National Yang-Ming Chaio-Tung University, Hsinchu 30010, Taiwan*

**Zih-Hao Song** − *Institute of NanoEngineering and MicroSystem, National Tsing-Hua University, Hsinchu 30013, Taiwan*

**Chih-Hsuan Liao** − *Institute of NanoEngineering and MicroSystem, National Tsing-Hua University, Hsinchu 30013, Taiwan*

**Quynh T. Dang** − *Department of Physics and Astronomy, University of California at Irvine, Irvine, California 92697, United States*

**Yu-Jung Lu** − *Research Center for Applied Sciences, Academia Sinica, Taipei 11529, Taiwan;* orcid.org/0000-0002-3932-653X

**Ho Wai Howard Lee** − *Department of Physics and Astronomy, University of California at Irvine, Irvine, California 92697, United States;* orcid.org/0000-0003-3962-3726

**Hyeyoung Ahn** − *Department of Photonics, National Yang-Ming Chaio-Tung University, Hsinchu 30010, Taiwan;* orcid.org/0000-0003-3209-6724

Complete contact information is available at: https://pubs.acs.org/10.1021/acs.jpcc.3c04763


### Notes

The authors declare no competing financial interest.


## ■ ACKNOWLEDGMENTS

This work was supported by the National Science and Technology Council (NSTC) in Taiwan under grant numbers NSTC 111-2123-M-007-002 and NSTC 110-2124-M-A49-009-MY3. We would like to acknowledge Yi-Jen Yu at Instrumentation Center, National Tsing-Hua University for TEM technical support. The TEM samples were fabricated by focused-ion beam milling (Hitachi NX2000) at Joint Center for High Valued Instruments at National Sun Yat-Sen University, Taiwan.


## ■ REFERENCES


(1) Faist, J.; Capasso, F.; Sivco, D. L.; Sirtori, C.; Hutchinson, A. L.; Cho, A. Y. Quantum Cascade Laser. *Science* **1994**, *264*, 553−556.

(2) Gol'tsman, G. N.; Okunev, O.; Chulkova, G.; Lipatov, A.; Semenov, A.; Smirnov, K.; Voronov, B.; Dzardanov, A.; Williams, C.; Sobolewski, R. Picosecond Superconducting Single-Photon Optical Detector. *Appl. Phys. Lett.* **2001**, *79*, 705−707.

(3) Wang, F.; Ren, F.; Ma, Z.; Qu, L.; Gourgues, R.; Xu, C.; Baghdasaryan, A.; Li, J.; Zadeh, I. E.; Los, J. W. N.; Fognini, A.; Qin-Dregely, J.; Dai, H. In Vivo Non-Invasive Confocal Fluorescence Imaging Beyond 1,700 nm Using Superconducting Nanowire Single-Photon Detectors. *Nat. Nanotechnol.* **2022**, *17*, 653−660.

(4) Lal, S.; Link, S.; Halas, N. J. Nano-Optics from Sensing to Waveguiding. *Nat. Photonics* **2007**, *1*, 641−648.

(5) Otte, M. A.; Sepúlveda, B.; Ni, W.; Juste, J. P.; Liz-Marzán, L. M.; Lechuga, L. M. Identification of the Optimal Spectral Region for Plasmonic and Nanoplasmonic Sensing. *ACS Nano* **2010**, *4*, 349−357.

(6) Sobhani, A.; Knight, M. W.; Wang, Y.; Zheng, B.; King, N. S.; Brown, L. V.; Fang, Z.; Nordlander, P.; Halas, N. J. Narrowband Photodetection in the Near-Infrared with a Plasmon-Induced Hot Electron Device. *Nat. Commun.* **2013**, *4*, 1643.

(7) Li, S. Q.; Guo, P.; Zhang, L.; Zhou, W.; Odom, T. W.; Seideman, T.; Ketterson, J. B.; Chang, R. P. H. Infrared Plasmonics with Indium-Tin-Oxide Nanorod Arrays. *ACS Nano* **2011**, *5*, 9161−9170.

(8) Stanley, R. Plasmonics in the Mid-Infrared. *Nat. Photonics* **2012**, *6*, 409−411.

(9) Low, T.; Avouris, P. Graphene Plasmonics for Terahertz to Mid-Infrared Applications. *ACS Nano* **2014**, *8*, 1086−1101.

(10) Rodrigo, D.; Limaj, O.; Janner, D.; Etezadi, D.; García de Abajo, F. J.; Pruneri, V.; Altug, H. Mid-Infrared Plasmonic Biosensing with Graphene. *Science* **2015**, *349*, 165−168.

(11) Zhong, Y.; Malagari, S. D.; Hamilton, T.; Wasserman, D. Review of Mid-Infrared Plasmonic Materials. *J. Nanophotonics* **2015**, *9*, 093791.

(12) Güsken, N. A.; Lauri, A.; Li, Y.; Matsui, T.; Doiron, B.; Bower, R.; Regoutz, A.; Mihai, A.; Petrov, P. K.; Oulton, R. F.; Cohen, L. F.; Maier, S. A. $TiO_{2-x}$ Enhanced IR Hot Carrier Based Photodetection in Metal Thin Film-Si Junctions. *ACS Photonics* **2019**, *6*, 953−960.

(13) Naik, G. V.; Shalaev, V. M.; Boltasseva, A. Alternative Plasmonic Materials: Beyond Gold and Silver. *Adv. Mater.* **2013**, *25*, 3264−3294.

(14) Naik, G. V.; Schroeder, J. L.; Ni, X.; Kildishev, A. V.; Sands, T. D.; Boltasseva, A. Titanium Nitride as a Plasmonic Material for Visible and Near-Infrared Wavelengths. *Opt. Mater. Express* **2012**, *2*, 478−489.

(15) Metaxa, C.; Kassavetis, S.; Pierson, J. F.; Gall, D.; Patsalas, P. Infrared Plasmonics with Conductive Ternary Nitrides. *ACS Appl. Mater. Interfaces* **2017**, *9*, 10825−10834.

(16) Patsalas, P.; Kalfagiannis, N.; Kassavetis, S.; Abadias, G.; Bellas, D. V.; Lekka, Ch.; Lidorikis, E. Conductive Nitrides: Growth Principles, Optical and Electronic Properties, and Their Perspectives in Photonics and Plasmonics. *Mater. Sci. Eng., R* **2018**, *123*, 1−55.

(17) Guo, W.-P.; Mishra, R.; Cheng, C.-W.; Wu, B.-H.; Chen, L.-J.; Lin, M.-T.; Gwo, S. Titanium Nitride Epitaxial Films as a Plasmonic Material Platform: Alternative to Gold. *ACS Photonics* **2019**, *6*, 1848−1854.

(18) Maniyara, R. A.; Rodrigo, D.; Yu, R.; Canet-Ferrer, J.; Ghosh, D. S.; Yongsunthon, R.; Baker, D. E.; Rezikyan, A.; García de Abajo, F. J.; Pruneri, V. Tunable Plasmons in Ultrathin Metal Films. *Nat. Photonics* **2019**, *13*, 328−333.

(19) Abd El-Fattah, Z. M.; Mkhitaryan, V.; Brede, J.; Fernández, L.; Li, C.; Guo, Q.; Ghosh, A.; Echarri, A. R.; Naveh, D.; Xia, F.; Ortega, J. E.; García de Abajo, F. J. Plasmonics in Atomically Thin Crystalline Silver Films. *ACS Nano* **2019**, *13*, 7771−7779.

(20) Gui, L.; Bagheri, S.; Strohfeldt, N.; Hentschel, M.; Zgrabik, C. M.; Metzger, B.; Linnenbank, H.; Hu, E. L.; Giessen, H. Nonlinear Refractory Plasmonics with Titanium Nitride Nanoantennas. *Nano Lett.* **2016**, *16*, 5708−5713.

(21) Guler, U.; Boltasseva, A.; Shalaev, V. M. Refractory Plasmonics. *Science* **2014**, *344*, 263−264.

(22) Kumar, M.; Umezawa, N.; Ishii, S.; Nagao, T. Examining the Performance of Refractory Conductive Ceramics as Plasmonic Materials: A Theoretical Approach. *ACS Photonics* **2016**, *3*, 43−50.

(23) Catellani, A.; Calzolari, A. Plasmonic Properties of Refractory Titanium Nitride. *Phys. Rev. B* **2017**, *95*, 115145.

(24) Maurya, K. C.; Shalaev, V. M.; Boltasseva, A.; Saha, B. Reduced Optical Losses in Refractory Plasmonic Titanium Nitride Thin Films Deposited with Molecular Beam Epitaxy. *Opt. Mater. Express* **2020**, *10*, 2679−2692.

(25) Mishra, R.; Chang, C.-W.; Dubey, A.; Chiao, Z.-Y.; Yen, T.-J.; Howard Lee, H. W.; Lu, Y. J.; Gwo, S. Optimized Titanium Nitride Epitaxial Film for Refractory Plasmonics and Solar Energy Harvesting. *J. Phys. Chem. C* **2021**, *125*, 13658−13665.

(26) Mishra, R.; Dubey, A.; Chang, C.-W.; Ranjan, A.; Lu, M.-Y.; Yen, T.-J.; Gwo, S. Epitaxial TiN/GaN Heterostructure for Efficient Photonic Energy Harvesting. *ACS Photonics* **2022**, *9*, 1895−1901.

(27) He, W.; Ai, K.; Jiang, C.; Li, Y.; Song, X.; Lu, L. Plasmonic Titanium Nitride Nanoparticles for *In Vivo* Photoacoustic Tomography Imaging and Photothermal Cancer Therapy. *Biomaterials* **2017**, *132*, 37−47.

(28) Qiu, G.; Ng, S. P.; Wu, C.-M. L. Label-Free Surface Plasmon Resonance Biosensing with Titanium Nitride Thin Film. *Biosens. Bioelectron.* **2018**, *106*, 129−135.
(29) Saha, B.; Shakouri, A.; Sands, T. D. Rocksalt nitride metal/semiconductor superlattices: A new class of artificially structured materials. *Appl. Phys. Rev.* **2018**, *5*, 021101.
(30) Lemasters, R.; Zhang, C.; Manjare, M.; Zhu, W.; Song, J.; Urazhdin, S.; Lezec, H. J.; Agrawal, A.; Harutyunyan, H. Ultrathin Wetting Layer-Free Plasmonic Gold Films. *ACS Photonics* **2019**, *6*, 2600−2606.
(31) Quynh, L. T.; Cheng, C.-W.; Huang, C.-T.; Raja, S. S.; Mishra, R.; Yu, M.-J.; Lu, Y.-J.; Gwo, S. Flexible Plasmonics Using Aluminum and Copper Epitaxial Films on Mica. *ACS Nano* **2022**, *16*, 5975−5983.
(32) Shah, D.; Reddy, H.; Kinsey, N.; Shalaev, V. M.; Boltasseva, A. Optical Properties of Ultrathin Plasmonic TiN Films. *Adv. Opt. Mater.* **2017**, *5*, 1700065.
(33) Shah, D.; Catellani, A.; Reddy, H.; Kinsey, N.; Shalaev, V.; Boltasseva, A.; Calzolari, A. Controlling the Plasmonic Properties of Ultrathin TiN Films at the Atomic Level. *ACS Photonics* **2018**, *5*, 2816−2824.
(34) Roberts, A. S.; Chirumamilla, M.; Wang, D.; An, L.; Pedersen, K.; Mortensen, N. A.; Bozhevolnyi, S. I. Ultra-thin titanium nitride films for refractory spectral selectivity [Invited]. *Opt. Mater. Express* **2018**, *8*, 3717−3728.
(35) Minn, K.; Anopchenko, A.; Chang, C. W.; Mishra, R.; Kim, J.; Zhang, Z.; Lu, Y. J.; Gwo, S.; Lee, H. W. H. Enhanced Spontaneous Emission of Monolayer $MoS_2$ on Epitaxially Grown Titanium Nitride Epsilon-Near-Zero Thin Films. *Nano Lett.* **2021**, *21*, 4928−4936.
(36) Ho, I.-H.; Chang, C.-W.; Chen, Y.-L.; Chang, W.-Y.; Kuo, T.-J.; Lu, Y.-J.; Gwo, S.; Ahn, H. Ultrathin TiN Epitaxial Films as Transparent Conductive Electrodes. *ACS Appl. Mater. Interfaces* **2022**, *14*, 16839−16845.
(37) Braic, L.; Vasilantonakis, N.; Mihai, A.; Villar Garcia, I. J.; Fearn, S.; Zou, B.; Alford, N. M.; Doiron, B.; Oulton, F.; Maier, S. A.; Zayats, A. V.; Petrov, P. K. Titanium Oxynitride Thin Films with Tunable Double Epsilon-Near-Zero Behavior for Nanophotonic Applications. *ACS Appl. Mater. Interfaces* **2017**, *9*, 29857−29862.
(38) Liberal, I.; Engheta, N. The Rise of Near-Zero-Index Technologies. *Science* **2017**, *358*, 1540−1541.
(39) Campione, S.; Brener, I.; Marquier, F. Theory of Epsilon-Near-Zero Modes in Ultrathin Films. *Phys. Rev. B: Condens. Matter Mater. Phys.* **2015**, *91*, 121408R.
(40) Alam, M. Z.; De Leon, I.; Boyd, R. W. Large Optical Nonlinearity of Indium Tin Oxide in Its Epsilon-Near-Zero Region. *Science* **2016**, *352*, 795−797.
(41) Kinsey, N.; DeVault, C.; Boltasseva, A.; Shalaev, V. M. Near-Zero-Index Materials for Photonics. *Nat. Rev. Mater.* **2019**, *4*, 742−760.
(42) Campione, S.; Liu, S.; Benz, A.; Klem, J. F.; Sinclair, M. B.; Brener, I. Epsilon-Near-Zero Modes for Tailored Light-Matter Interaction. *Phys. Rev. Appl.* **2015**, *4*, 044011.
(43) Shockley, W.; Queisser, J. Detailed Balance Limit of Efficiency of *p-n* Junction Solar Cells. *J. Appl. Phys.* **1961**, *32*, 510−519.
(44) Swanson, R. M. A Proposed Thermophotovoltaic Solar Energy Conversion System. *Proc. IEEE* **1979**, *67*, 446−447.
(45) Fan, S. An Alternative "Sun" for Solar Cells. *Nat. Nanotechnol.* **2014**, *9*, 92−93.
(46) Lenert, A.; Bierman, D. M.; Nam, Y.; Chan, W. R.; Celanović, I.; Soljačić, M.; Wang, E. N. A Nanophotonic Solar Thermophotovoltaic Device. *Nat. Nanotechnol.* **2014**, *9*, 126−130.
(47) Wang, Y.; Liu, H.; Zhu, J. Solar Thermophotovoltaics: Progress, Challenges, and Opportunities. *APL Mater.* **2019**, *7*, 080906.
(48) Harder, N. P.; W rfel, P. Theoretical limits of thermophotovoltaic solar energy conversion. *Semicond. Sci. Technol.* **2003**, *18*, S151−S157.
(49) Rephaeli, E.; Fan, S. Absorber and Emitter for Solar Thermo-Photovoltaic Systems to Achieve Efficiency Exceeding the Shockley-Queisser Limit. *Opt. Express* **2009**, *17*, 15145−15159.
(50) Wang, Q.; Hou, G.; Zhu, Y.; Sun, T.; Xu, J.; Chen, K. Nanolayered Wavelength-Selective Narrowband Thermal Emitters for Solar Thermophotovoltaics. *ACS Appl. Nano Mater.* **2022**, *5*, 13455−13462.


https://doi.org/10.1021/acs.jpcc.3c04763
J. Phys. Chem. C 2023, 127, 21186−21193